nature materials

ARTICLES

PUBLISHED ONLINE: 21 AUGUST 2011 | DOI: 10.1038/NMAT3098

Interface-induced room-temperature multiferroicity in $BaTiO_3$

S. Valencia[1], A. Crassous[2], L. Bocher[3], V. Garcia[2], X. Moya[4], R. O. Cherifi[2], C. Deranlot[2], K. Bouzehouane[2], S. Fusil[2,5], A. Zobelli[3], A. Gloter[3], N. D. Mathur[4], A. Gaupp[1], R. Abrudan[6], F. Radu[1], A. Barthélémy[2] and M. Bibes[2]*

Multiferroic materials possess two or more ferroic orders but have not been exploited in devices owing to the scarcity of room-temperature examples. Those that are ferromagnetic and ferroelectric have potential applications in multi-state data storage if the ferroic orders switch independently, or in electric-field controlled spintronics if the magnetoelectric coupling is strong. Future applications could also exploit toroidal moments and optical effects that arise from the simultaneous breaking of time-reversal and space-inversion symmetries. Here, we use soft X-ray resonant magnetic scattering and piezoresponse force microscopy to reveal that, at the interface with Fe or Co, ultrathin films of the archetypal ferroelectric $BaTiO_3$ simultaneously possess a magnetization and a polarization that are both spontaneous and hysteretic at room temperature. *Ab initio* calculations of realistic interface structures provide insight into the origin of the induced moments and bring support to this new approach for creating room-temperature multiferroics.

In a seminal paper published in 2000, Nicola Spaldin (then Hill) asked the question "Why are there so few magnetic ferroelectrics?"[1]. She observed that perovskite ferroelectrics have d^0 ions, whereas magnetism requires partially filled d (or f) shells, making a further electronic or structural driving force necessary for ferromagnetism and ferroelectricity to occur simultaneously. This seemed at the time both intriguing and stimulating for the nascent community investigating multiferroics, so much so that the field has grown exponentially since then. In subsequent years, novel mechanisms for ferroelectricity have been discovered in magnetic insulators[2], causing a spectacular increase in the number of actual multiferroics[3–5].

However, the quest for materials showing ferromagnetism and ferroelectricity at room temperature remains a major challenge, the solution of which could unlock technological advances in numerous fields. For instance, multiferroics showing strong magnetoelectric coupling could lead to spin-based devices with ultralow power consumption[6–8] and novel microwave components[9]. In the case of independent switching of the ferroic order parameters, multiferroics could also find applications as multiple-state data storage elements[10] or multifunctional photonic devices exploiting non-reciprocal optical effects[11,12].

To tackle this enduring challenge, various approaches have been proposed. These include chemical substitution in the room-temperature ferroelectric antiferromagnet $BiFeO_3$ (ref. 13), strain engineering[14], or the combination of ferroelectrics and ferromagnetic materials with high ordering temperatures to design composite (or 'artificial') multiferroics, usually in the form of ceramics or self-organized nanostructures[15]. However, a practical room-temperature ferroelectric ferromagnet remains elusive.

Another strategy aims at exploiting electronic structure changes at interfaces between a ferromagnet and a ferroelectric. First-principles calculations on prototypical systems such as $Fe/BaTiO_3$ (refs 16–18) have predicted that charge redistribution at the interface may cause the ferromagnet to become sensitive to the ferroelectric polarization direction and, reciprocally, may induce finite magnetic moments in the ferroelectric. In theory, such interfacial multiferroics therefore exhibit magnetoelectric coupling and interface-induced multiferroicity, both at room temperature, if robust ferroics such as Fe and $BaTiO_3$ are combined. Interfacial multiferroics thus emerge as particularly promising to circumvent the lingering scarcity of single-phase room-temperature multiferroics[19].

In this paper we demonstrate both interfacial magnetoelectric coupling and room-temperature interface-induced multiferroicity in $Fe/BaTiO_3$ and $Co/BaTiO_3$ heterostructures. More specifically, we report ferroelectricity-controlled tunnel magnetoresistance (TMR) in artificial multiferroic tunnel junctions ($Fe/BaTiO_3$/LSMO and $Co/BaTiO_3$/LSMO) (LSMO stands for $La_{2/3}Sr_{1/3}MnO_3$) as well as the observation of a remanent magnetic moment in ferroelectric $BaTiO_3$ (BTO), at the interface with Fe and Co, at 300 K. We provide direct evidence for a ferromagnetic-like behaviour through element selective X-ray resonant magnetic scattering (XRMS) spectra and hysteresis loops obtained at the Ti $L_{3,2}$- and O K-edges. For the Fe/BTO system, we compute the magnetic moments of a realistic interface (inferred from atomically resolved scanning transmission electron studies) to shed light on the origin of the dichroic signal on formally non-magnetic ions such as Ti^{4+}. We suggest that ferromagnetism can be induced without Ti^{3+} just as a result of iono-covalency effects with neighbouring spin-polarized O and Fe atoms.

[1]Helmholtz-Zentrum-Berlin für Materialen und Energie, Albert-Einstein-Strasse 15, 12489 Berlin, Germany, [2]Unité Mixte de Physique CNRS/Thales, 1 Avenue Augustin Fresnel, Campus de l'Ecole Polytechnique, 91767 Palaiseau, France, and Université Paris-Sud, 91405 Orsay, France, [3]Laboratoire de Physique des Solides, Université Paris-Sud, CNRS UMR-8502, 91405 Orsay, France, [4]Department of Materials Science, University of Cambridge, Cambridge CB2 3QZ, UK, [5]Université d'Evry-Val d'Essonne, Boulevard François Mitterrand, 91025 Evry cedex, France, [6]Institut für Experimentalphysik/Festkörperphysik, Ruhr-Universität Bochum, 44780 Bochum, Germany. *e-mail: manuel.bibes@thalesgroup.com.

© 2011 Macmillan Publishers Limited. All rights reserved

For this study we used Fe/BTO/LSMO(30 nm)//NGO(001) and Co/BTO/LSMO(30 nm)//NGO(001) samples (NGO stands for $NdGaO_3$; ref. 20) capped by either AlO_x (1.5 nm)/Al(1.5 nm)—for spectroscopy measurements—or by a Au/CoO/Co stack for magnetotransport. For X-ray absorption spectroscopy (XAS) and XRMS experiments, the Fe, Co and BTO thicknesses were set to 2 nm, 2 nm and 1.2 nm, respectively and the BTO was unpoled. Previous X-ray diffraction experiments and cross-section TEM analysis[20] indicated that our BTO ultrathin films are (001) oriented (that is, with the polarization perpendicular to the sample plane). Structural and piezoresponse force microscopy (PFM) measurements indicate a multidomain configuration in the virgin state with nanoscale domains with polarization pointing either up or down. Selected heterostructures were investigated using a spherical-aberration-corrected scanning transmission electron microscope (STEM). STEM high-angle annular dark-field (HAADF) images showed that the BTO is epitaxial[20] whereas the Fe (ref. 21) and Co layers consist of textured crystallites. X-ray absorption data confirmed the chemical quality of the bottom LSMO layer as well as that of the BTO ferroelectric barrier[21]. The Fe and Co $L_{3,2}$-edge XAS and X-ray magnetic circular dichroism (XMCD) spectra corresponding to the top layers are shown in Fig. 2a,d. Apart from a small signature from the Ba $M_{5,4}$ edge visible in the Co XAS data, the spectra are typical of bulk bcc Fe (ref. 22) and hcp Co (ref. 22), respectively. We note, however, that from these data we cannot exclude the presence of an ultra-thin oxidized layer at the metal/BTO interface[23].

To probe the influence of ferroelectric polarization direction in BTO on the magnetic properties of the Fe and Co, we measured the TMR of Fe/BTO/LSMO and Co/BTO/LSMO tunnel junctions as a function of the ferroelectric polarization direction in the BTO tunnel barrier (after field cooling from 300 K to increase and shift the switching fields of the top magnetic electrodes owing to exchange bias[24] from the CoO layer). Figure 1a shows TMR curves collected at −50 mV and 10 K after consecutive poling at $V_p = -0.9$ V or +0.9 V to orient the ferroelectric polarization in BTO towards the LSMO or the Fe, respectively. The TMR is negative, which (within Jullière's model[25] and in view of the positive spin polarization of LSMO; ref. 26) signals a negative spin-polarization for the Fe/BTO interface, in agreement with first-principles predictions[16,17]. As expected when the tunnel barrier is ferroelectric, the junctions also exhibit tunnel electroresistance (TER; refs 20,27,28), that is, a variation of their resistance with polarization direction at fixed magnetic field.

More importantly, the TMR is found to depend strongly on the ferroelectric polarization direction, taking absolute values that are about twice as large when the polarization points towards Fe. These data confirm the results of ref. 21 and correspond to an average tunnel electromagnetoresistance effect (defined as TEMR $= (\mathrm{TMR}_{V_p^+} - \mathrm{TMR}_{V_p^-})/\mathrm{TMR}_{V_p^-}$ (ref. 21) of ∼150%. Figure 1b shows comparable results for the Co/BTO/LSMO system. Similarly, consecutive TMR curves measured at 200 mV and 4 K after poling at $V_p = -1$ V or +1 V show a strong influence of the ferroelectric polarization direction on the TMR effect (that is, also negative, in line with the predicted negative sign of spin-polarization at the Co/BTO interface[29] and previous Co/STO/LSMO TMR data[30]). The average TEMR here is ∼82%. These results can be interpreted as reflecting a modulation of the spin-polarization of Fe and Co at the interface with BTO with the direction of the ferroelectric polarization. In this sense they evidence a form of interfacial magnetoelectric coupling at the interface between the ferromagnet and the ferroelectric, consistent with the theoretical predictions of refs 16–18,29.

The corollary of the influence of ferroelectricity on magnetism at multiferroic interfaces is the generation of a magnetic moment in the ferroelectric by the ferromagnet. In the reports from Duan *et al.*[16] and Fechner *et al.*[17], the induced moments calculated

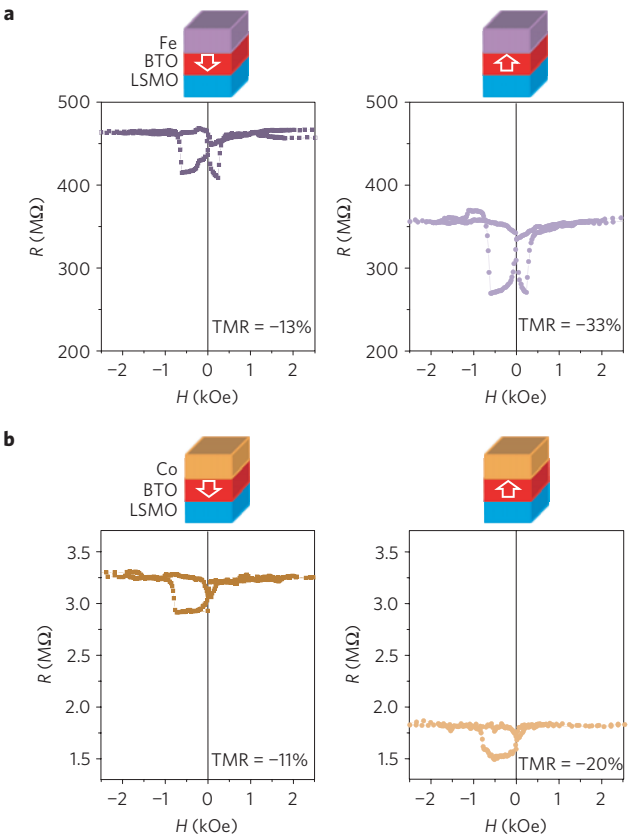

Figure 1 | Influence of ferroelectric polarization direction on TMR in Fe/BTO/LSMO and Co/BTO/LSMO junctions. a, Consecutive resistance versus magnetic field curves measured at 50 and 10 K on a Au/CoO/Co/Fe/BTO(1.2 nm)/LSMO tunnel junction after poling the BTO ferroelectric barrier down or up. **b**, Similar curves at 200 mV and 4 K on a Au/CoO/Co/BTO(2 nm)/LSMO junction. All curves were collected after cooling from 300 K in a field of 5 kOe.

for Ti and O in BTO at the interface with Fe (averaged over the two possible ferroelectric polarization directions) are approximately 0.1–0.2 μ_B/atom and 0.01–0.05 μ_B/atom, respectively. In this picture, the magnetic signal is expected to arise mainly from the very first BTO atomic layer in contact with the transition metal, and its detection by means of XMCD is challenging. It is well known that, owing to interference effects, the reflection counterpart of XMCD exhibits a higher sensitivity to interface magnetization[31] and therefore allows the detection of small magnetic moments not detectable by means of absorption techniques. In Fig. 2b,c the top panels show the XRMS spectra obtained at the O K-edge and Ti $L_{3,2}$-edge for the Fe/BTO sample and the bottom panels present the associated XRMS asymmetry (A_{XRMS}). This dichroic quantity is defined as $A_{\mathrm{XRMS}} = (R^+ - R^-)/(R^+ + R^-)$, $R^{+(-)}$ being the XRMS spectrum measured in remanence after magnetic saturation with a positive (negative) magnetic field. In the case of non-magnetic Ti or O atoms, R^+ and R^- are expected to be equal and, thus, $A_{\mathrm{XRMS}} = 0$. However, the data show a finite dichroism for Ti and O, thus evidencing the presence of magnetism. Although the dichroic signals are weak, they clearly reverse on changing the helicity of the light (see Fig. 2b,c, bottom panels), which confirms their magnetic origin. Figure 2e,f show XRMS and asymmetry spectra for the Co sample. As in the Fe/BTO case, a finite dichroic signal is clearly visible at the O K-edge and Ti $L_{3,2}$-edge (bottom panels). We note for the latter the enhancement of the A_{XRMS} at 466 eV. This large asymmetry (2%), as compared with the rest of the data (0.2%–0.4%), arises owing to interference effects as well as to

© 2011 Macmillan Publishers Limited. All rights reserved

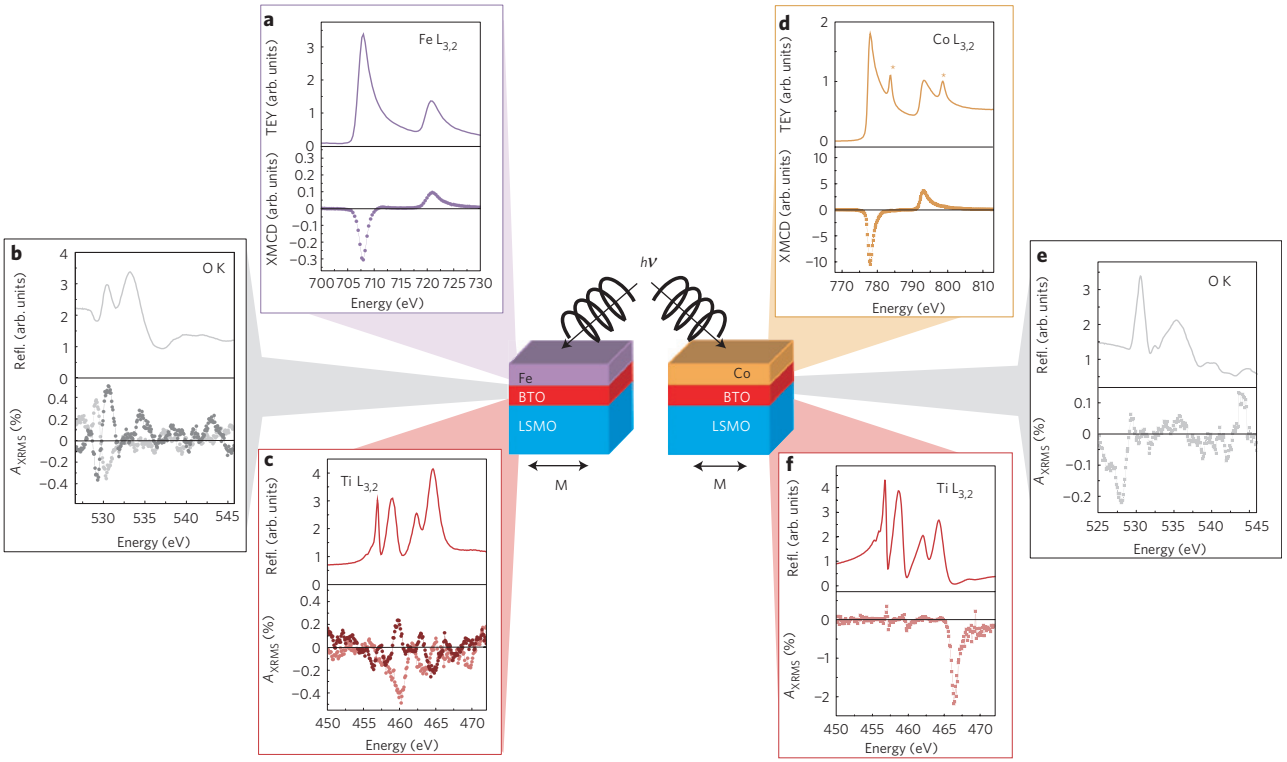

Figure 2 | Element specific magnetic signals at Fe/BTO and Co/BTO interfaces. a, Top: XAS spectrum for Fe; bottom: XMCD spectrum for Fe. **b**, Top: XRMS spectrum for O; bottom: XRMS asymmetry spectra for O obtained for right (dark grey) and left (light grey) helicities of the incoming circularly polarized radiation. **c**, Top: XRMS spectrum for Ti; bottom: XRMS asymmetry spectra for Ti obtained for right (dark red) and left (light red) helicities of the incoming circularly polarized radiation. **d**, Top: XAS spectrum for Co (stars indicate absorption at the Ba $M_{5,4}$ edge); bottom: XMCD spectrum for Co. **e**, Top: XRMS spectrum for O; bottom: XRMS asymmetry spectrum for O obtained for left circularly polarized radiation. **f**, Top: XRMS spectrum for Ti; bottom: XRMS asymmetry spectrum for Ti obtained for left circularly polarized radiation. All measurements were performed at 300 K.

the definition of A_{XRMS} that enhances dichroic effects at energies where the reflected intensity is minimum. As BTO is the only layer containing Ti atoms in both heterostructures, these data indicate the presence of finite magnetic moments in the BTO films in remanence and at room temperature.

To unambiguously demonstrate the ferromagnetic-like character of BTO, we have measured the dependence of the XRMS signals at selected energies as a function of the magnetic field. Figure 3a (Fe/BTO sample) and Fig. 3b (Co/BTO sample) show the results for Fe or Co, Ti and O as well as Mn (the reflectivity and A_{XRMS} spectra at the Mn $L_{3,2}$ edges are available in the Supplementary Information). All signals show clear hysteresis loops as a function of magnetic field. For the BTO/Co sample, all signals have virtually identical coercive fields, which could be coincidental, or indicate magnetic coupling of the LSMO and Co across the BTO film, with magnetism extending throughout the whole BTO thickness (1.2 nm). Interestingly, electric-field dependent magnetic coupling across ferroelectric films has indeed been predicted recently[32]. For the Fe/BTO sample, the Ti and O signals reverse at the same magnetic field as the Fe, whereas the Mn signal—and thus the magnetization of LSMO—reverses at a lower field. This indicates that the magnetic moments carried by the Ti and O ions are coupled to the Fe, as expected if the Ti and O moments are induced at the interface with the Fe layer in agreement with theory[16–18].

Figure 3c also shows the out-of-plane piezoresponse of a similar BTO(1.2 nm)/LSMO sample as a function of the applied voltage. The main panel shows the phase signal, with the amplitude and the extracted piezoelectric coefficient shown in the insets. This hysteretic piezoresponse confirms our inference of a ferroelectric character in similar ultrathin BTO films by PFM imaging[20], with finite piezoresponse at remanence, switchable by a d.c. voltage of ∼2 V (in absolute value). The concomitant observation of ferroelectricity and ferromagnetic-like behaviour in ultrathin BTO films attests their multiferroic character at room temperature.

To get a better insight into the origin of the observed magnetic signals, we have performed first-principles electronic-structure calculations of the interfacial magnetic moments using the interface structure determined from experimental investigations based on atomically resolved STEM-HAADF images of the Fe/BTO sample. Figure 4a shows a representative atomically resolved HAADF image of the Fe/BTO interface. The observed Fe/BTO interface structure seems more complex than expected in previous theoretical studies[16,17]. The HAADF image clearly presents a darker contrast between the magnetic film and the ferroelectric layer, indicating the presence of an interfacial phase thinner than ∼6 Å. Based on various types of interface structures, HAADF image simulations of the interface were essayed using the multislice method in the 'frozen-phonon' approach and further compared with the experimental HAADF images. Figure 4b shows the structural model that was found to be a better match to the image. In this model (which we refer to as type II henceforth), the first Fe atoms are not only hybridized with O ions in the growth direction (as in the models—type I—of refs 16,17) but also in the plane, which can also be seen as reflecting the presence of a FeO monolayer at the interface.

Density-functional calculations of the electronic and atomic structure were performed using the ABINIT code[33,34] (see Methods). Supercells were built up by aligning the [100] axis of the BTO with the body centred cubic iron [110] axis and two different interface models were investigated: $(Fe_2)_5$–TiO_2–$(BaO–TiO_2)_5$ (type I interface) as in refs 16,17 and $(Fe_2)_5$–FeO–TiO_2–$(BaO–TiO_2)_5$ (type

© 2011 Macmillan Publishers Limited. All rights reserved

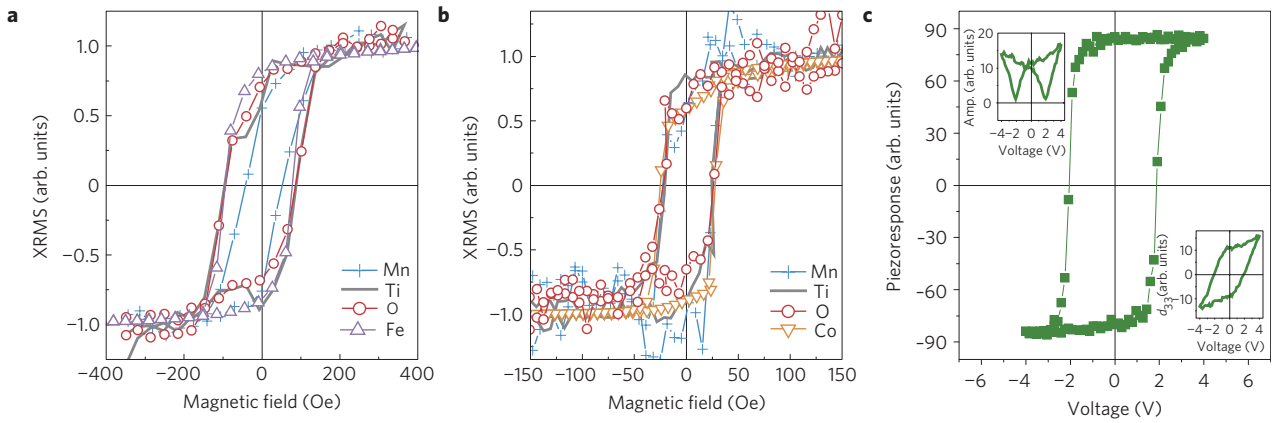

Figure 3 | Evidence for room-temperature multiferroicity. a, XRMS versus H for Mn, Fe, Ti and O for the Fe/BTO sample. **b**, XRMS versus H for Mn, Co, Ti and O for the Co/BTO sample. **c**, Out-of-plane piezoresponse phase loop of a BTO(1.2 nm)/LSMO sample. The corresponding amplitude and extracted piezoelectric coefficient (d_{33}) data are shown in the insets.

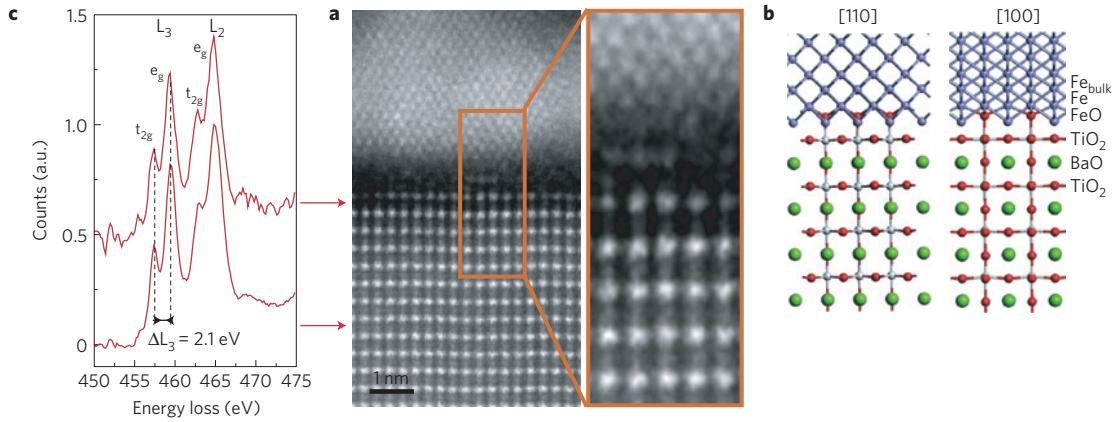

Figure 4 | Interface structure analysis. a, Atomically resolved HAADF image of the Fe/BTO interface of the Fe/BTO(50 nm)/LSMO(30 nm)//NGO(001) heterostructure. **b**, Structural model of the type II interface, that is, -Fe-FeO-TiO_2-$BaTiO_3$. **c**, Ti $L_{2,3}$-edge spectra acquired on TiO_2 columns located in the BTO layer (blue line) and next to the Fe layer (red line).

II interface) as schematically presented in Fig. 4b. Table 1 gathers the magnetic moments calculated (and averaged over the two possible ferroelectric polarization directions) for both interface types. In both cases, we obtain a moment of ~2.06 μ_B/atom for Fe atoms far from the interface. This is slightly lower than the expected value of 2.20 μ_B/atom (ref. 16), which may be related to strain effects on the Fe bcc cell imposed in the calculations. For the type I interface, we calculate an enhanced Fe interfacial moment, qualitatively consistent with ref. 16. The interfacial Ti and O ions possess significant moments of −0.14 μ_B/atom and 0.05 μ_B/atom, respectively, which agree in sign with the results of both Duan *et al.*[16] and Fechner *et al.*[17], and fall within the range of values found by these authors. The good agreement with literature data can be considered as a validation of our computational approach.

Table 1 also presents the calculated averaged moments for the type II interface that corresponds better to the real structure of our samples. Both Fe and O in the interfacial FeO layer carry large moments of 2.80 μ_B/atom and 0.17 μ_B/atom, respectively. The Fe atoms in the adjacent Fe plane have a moment of 2.35 μ_B/atom. As for the type I case, the Ti and O ions at the interface have sizeable negative (−0.07 μ_B/atom) and positive (0.05 μ_B/atom) moments, respectively. Interestingly, the Ti ions in the second BTO plane have moments only reduced by a factor of ~2 with respect to those in the interface BTO plane, and are significantly larger than their equivalents for the type I interface.

In agreement with the experimental results, the calculations for the type II interface indicate that the Ti ions in the BTO should have a magnetic moment. To better understand its origin, a Fe/BTO/LSMO heterostructure was further investigated by means of electron energy loss spectroscopy (EELS) to locally probe the fine structure of the Ti $L_{3,2}$-edge (see Methods) in the BTO away from and just at the interface with the Fe layer. Figure 4c shows Ti $L_{3,2}$-edge spectra acquired from atomic columns (1) at a TiO_2 monolayer in the BTO barrier eight unit-cells from the interface and (2) just at the interface with Fe. Both spectra present very similar features, in line with the density functional theory (DFT) results that indicate comparable *d* orbital occupation for Ti atoms deep in the BTO and at the interface. As revealed by a recent EELS study on bulk Ti^{4+}/Ti^{3+} mixed-valence compounds[35], the presence of less than 20% of Ti^{3+} does not massively alter the Ti $L_{3,2}$-edge fine structure, making a direct determination of the Ti valence difficult. However, the different energy splittings observed in the EELS spectra, namely, the 2*p* spin–orbit coupling giving rise to the two main L_3 and L_2 peaks, and the splitting between the non-degenerate energy levels (t_{2g} and e_g) for each edge, are characteristic of a primary Ti^{4+} ion[35]. X-ray absorption spectra are also typical of Ti^{4+} (ref. 20).

The present DFT calculations show that a charge transfer of around 0.2 electrons occurs from Fe to the interfacial Ti *d* band in the ideal TiO_2-terminated Fe/BTO structural model (type I). These extra electrons are located close to the Fermi

© 2011 Macmillan Publishers Limited. All rights reserved

Table 1 | *Ab initio* calculated moments for Fe, Ti, Ba and O at the Fe/BTO interface.

Type I interface (...-Fe-TiO_2-BaO-TiO_2-...)

Atomic planes	Atoms	Magnetic moment (μ_B)	Atoms	Magnetic moment (μ_B)
Fe bulk	Fe	2.06		
Fe	Fe	2.23		
TiO_2	Ti	−0.15	O	0.04
BaO	Ba	<0.01	O	<0.01
TiO_2	Ti	−0.02	O	<0.01

Type II interface (...-Fe-FeO-TiO_2-BaO-TiO_2-...)

Atomic planes	Atoms	Magnetic moment (μ_B)	Atoms	Magnetic moment (μ_B)
Fe bulk	Fe	2.07		
Fe	Fe	2.35		
FeO	Fe	2.80	O	0.17
TiO_2	Ti	−0.07	O	0.05
BaO	Ba	<0.01	O	0.01
TiO_2	Ti	−0.03	O	<0.01

level, as previously evidenced by Duan *et al.*[16], and are efficiently spin-polarized by direct hybridization with the Fe, giving a total magnetic moment of around 0.15 μ_B. In contrast, almost no charge transfer occurs towards the Ti *d* band in the case of the type II interface, which can be easily understood by considering the full oxygen octahedra environment of the interfacial Ti atom in this structural model. This theoretical evidence reinforces the sole presence of Ti^{4+} at the interface. The magnetic moment seems to be mostly carried by the O and Fe of the FeO interfacial layer. Nevertheless, the Ti atoms at and next to the interface are also spin-polarized through a hybridization scheme with Fe and spin-polarized oxygen atoms, resulting in a finite magnetic moment as well. This mechanism is therefore different from the one invoked by Garcia-Barriocanal *et al.*[36] to interpret the dichroic signal observed at the Ti $L_{3,2}$-edge in $LaMnO_3/SrTiO_3$ superlattices, which considers charge transfer from $LaMnO_3$ to $SrTiO_3$, resulting in a strong reduction of the Ti valence toward 3+. Although we cannot completely rule out that this latter scenario may also make a marginal contribution, the dominant mechanism here is similar to the one proposed to explain magnetism by means of covalent effects between Ti and neighbouring spin-polarized O and Fe atoms in formally Ti^{4+} ions in $FeTiO_3$ (ref. 37) and Fe_2TiO_4 (ref. 38). We also stress that the mechanism at play here is different from the one invoked to explain enhanced magnetism below about 100 K at $BiFeO_3$/LSMO interfaces (ascribed to orbital reconstruction)[39] or in $La_{2/3}Ca_{1/3}MnO_3/La_{1/3}Ca_{2/3}MnO_3$ heterostructures (due to competing exchange interactions)[40].

In summary, we have found that the spin-polarization of Fe/BTO and Co/BTO interfaces can be controlled by the direction of ferroelectric polarization in BTO, and detected for both cases a spontaneous and hysteresis magnetic moment in BTO. This indicates that a multiferroic character may be generated in a nominally diamagnetic ferroelectric at room temperature. The most likely mechanism at play here involves formally Ti^{4+} ions and a spin-polarized iono-covalent bonding scheme with atoms in the adjacent ferromagnet. This expands the possibilities for multiferroic and/or magnetoelectric interface engineering and invites a reassessment of the general trends for the exploration of multiferroic systems. Our results indicate that magnetism extends over several unit-cells in the ferroelectric layer, opening the way towards artificial multiferroic tunnel barriers[10] that would be relevant for room-temperature storage and logic devices[41,42]. As the coexistence of spontaneous magnetization and polarization implies time-reversal and space-inversion breaking in zero-field, such novel interface-induced multiferroics could exhibit exciting non-reciprocal optical effects[11,12] and ferrotoroidic order[43]. Finally, our finding can also be taken as the first evidence for spin-polarized metal-induced gap states in tunnel barriers in contact with transition metal ferromagnets, which were theoretically predicted several years ago[44] but had remained undetected directly until now[45].

Methods

BTO/LSMO bilayers were grown by pulsed laser deposition on (001) $NdGaO_3$(NGO) substrates using a KrF laser ($\lambda = 248$ nm) with a fluence of 2 J cm^{-2} and a repetition rate of 1 Hz. This substrate was chosen to induce a large compressive strain in ultrathin films of BTO, which increases the ferroelectric polarization significantly. 30 nm LSMO films were grown at a deposition temperature of 775 °C and an oxygen pressure of 0.15 mbar. The subsequent growth of BTO with an oxygen pressure of 0.10 mbar was followed by 1 h annealing at 750 °C in a high oxygen pressure (500 mbar) to avoid oxygen vacancies in the tunnel barrier. The Fe layers were grown by RF sputtering at room temperature and covered by a naturally oxidized Al layer, resulting in a AlO_x (1.5 nm)/Al(1.5 nm) cap. The tunnel junctions were defined by nanoindentation lithography[46,47] with top electrodes of either Au/CoO/Co or Au/CoO/Co/Fe (see also ref. 26 for details on the role of CoO).

Piezoresponse force microscopy experiments were performed using a commercial atomic force microscope (MFP-3D Asylum) in DART (dual AC resonance tracking)[48] mode on BTO (1.2 nm)/LSMO//NGO samples. Commercial Si tips coated with Cr/Pt (Budget Sensors TAP 300 E) were used at typical contact resonance frequencies of 1.2 MHz with a nominal a.c. voltage of 1 V peak to peak.

Soft X-ray magnetic absorption and scattering measurements were performed at room temperature using the ALICE diffractometer[49] installed at the PM3 beam line of the HZB-BESSY II synchrotron radiation source in Berlin, Germany. The polarization of the incoming radiation was set to circular (Pc = 0.92(3)) for the XAS, XMCD and XRMS experiments. Absorption was simultaneously measured by means of total electron yield (TEY) and fluorescence yield (FY) in the case of Fe/BTO, and by means of TEY only for Co/BTO. The radiation impinged the sample at an angle of 20° along the incoming beam propagation direction (Supplementary Fig. S1). For reflection, the sample was placed at incidence angles of 10° and 15° with respect to the incoming propagation direction. The following edges within the soft X-ray range were measured: the O K-edge, and the Mn, Fe and Ti $L_{3,2}$ edges. The XMCD and A_{XRMS} spectra were obtained for a fixed helicity of the incoming polarization by reversing the magnetization direction at every data point from positive to negative by means of an external magnetic field (±0.1 T). This set-up optimizes the signal to noise ratio, allowing the detection of very small dichroic effects. To avoid the influence of the magnetic field on the TEY acquisition, data were obtained in remanence. XMCD is defined as the difference between the two absorption curves (+0.1 and −0.1 T) whereas A_{XRMS} is defined as the difference of the two reflection curves (+0.1 and −0.1 T) normalized by their sum. XRMS hysteresis loops have been obtained at an incidence angle of $\theta = 10°$ from the surface. The helicity of the incoming circularly polarized beam was fixed during data acquisition (Supplementary Fig. S2).

Cross-sections of two Fe/BTO/LSMO//NGO heterostructures (with a BTO thickness of 50 and 3.5 nm) were first prepared by the tripod method for the mechanical polishing and further thinned to electron transparency with a precision ion-polishing system. STEM-HAADF images were acquired using a C3/C5 aberration-corrected STEM, in this case the NION UltraSTEM 100 kV with a probe size of 1 Å, allowing an atomic resolution and coupled with EELS experiments performed with a collection semi-angle of 30 mrad and a convergence semi-angle of 35 mrad at a current of approximately 110 pA. These experimental parameters enabled us to probe the 3*d* transition metal fine structure in the perovskite structure atomic column by atomic column. The EELS spectra were acquired using the spectrum line mode, with an energy dispersion of 0.2 eV/channel and an acquisition time of 1 s. Very similar results were obtained for both samples, with slightly higher quality images and spectra for the BTO(50 nm) sample owing to better experimental conditions.

DFT calculations were performed using the plane wave basis (energy cut-off of 50 Ha), pseudo-potential approach (with nonlinear core correction) and the local spin density approximation (LSDA). The atomic relaxation calculations were performed using a $4 \times 4 \times 1$ supercell including a shift of $0.1 \times 0.1 \times 0.2$ grid *k*-point sampling and atomic positions were adjusted until the forces on each atoms converged to less than 5×10^{-2} Ha/Bohr. First, separate atomic relaxation calculations of the bulk Fe and BTO structures were performed applying these in-plane constraint parameters, and then used as structural inputs for constructing supercells which were further structurally relaxed. In both interface models, the perovskite structure consists of the typical $AO-BO_2$ stacking sequence terminating with TiO_2 atomic planes, as previously reported to be the most stable termination[16].

© 2011 Macmillan Publishers Limited. All rights reserved

Received 14 February 2011; accepted 12 July 2011; published online 21 August 2011

References

1. Hill, N. A. Why are there so few magnetic ferroelectrics? *J. Phys. Chem. B.* **104,** 6694–6709 (2000).
2. Cheong, S-W. & Mostovoy, M. Multiferroics: A magnetic twist for ferroelectricity. *Nature Mater.* **6,** 13–20 (2007).
3. Eerenstein, W., Mathur, N. D. & Scott, J. F. Multiferroic and magnetoelectric materials. *Nature* **442,** 759–765 (2006).
4. Béa, H., Gajek, M., Bibes, M. & Barthélémy, A. Spintronics with multiferroics. *J. Phys.: Condens. Matter* **20,** 434221 (2008).
5. Bibes, M., Villlegas, J. E. & Barthélémy, A. Ultrathin oxide films and interfaces for electronics and spintronics. *Adv. Phys.* **60,** 5–84 (2011).
6. Binek, C. & Doudin, B. Magnetoelectronics with magnetoelectrics. *J. Phys.: Condens. Matter.* **17,** L39–L44 (2005).
7. Chu, Y-H. *et al.* Electric-field control of local ferromagnetism using a magnetoelectric multiferroic. *Nature Mater.* **7,** 478–482 (2008).
8. Bibes, M. & Barthélémy, A. Towards a magnetoelectric memory. *Nature Mater.* **7,** 425–426 (2008).
9. Wood, V. E & Austin, A. E. in *Magnetoelectric Interaction Phenomena in Crystals* (eds Freeman, A. J. & Schmid, H.) (Gordon and. Breach, 1975).
10. Gajek, M. *et al.* Tunnel junctions with multiferroic barriers. *Nature Mater.* **6,** 296–302 (2007).
11. Rikken, G. L. J. A. & Raupach, E. Observation of magneto-chiral dichroism. *Nature* **390,** 493–494 (1997).
12. Sawada, K. & Nagaosa, N. Optical magnetoelectric effect in multiferroic materials: Evidence for a Lorentz force acting on a ray of light. *Phys. Rev. Lett.* **95,** 237402 (2005).
13. Catalan, G. & Scott, J. F. Physics and applications of bismuth ferrite. *Adv. Mater.* **21,** 2463–2485 (2009).
14. Lee, J. H. *et al.* A strong ferroelectric ferromagnet created by means of spin-lattice coupling. *Nature* **466,** 954–958 (2010).
15. Hu, J., Li, J. & Nan, C-W. Recent progress in multiferroic magnetoelectric composites: From bulk to thin films. *Adv. Mater.* **23,** 1062–1087 (2011).
16. Duan, C-G., Jaswal, S. S. & Tsymbal, E. Y. Predicted magnetoelectric effect in Fe/$BaTiO_3$ multilayers: Ferroelectric control of magnetism. *Phys. Rev. Lett.* **97,** 047201 (2006).
17. Fechner, M. *et al.* Magnetic phase transition in two-phase multiferroics predicted from first principles. *Phys. Rev. B* **78,** 212406 (2008).
18. Lee, J., Sai, N., Cai, T., Niu, Q. & Demkov, A. A. Interfacial magnetoelectric coupling in tricomponent superlattices. *Phys. Rev. B* **81,** 144425 (2010).
19. Kitagawa, Y. *et al.* Low-field magnetoelectric effect at room temperature. *Nature Mater.* **9,** 797–802 (2010).
20. Garcia, V. *et al.* Giant tunnel electroresistance for non-destructive readout of ferroelectric states. *Nature* **460,** 81–84 (2009).
21. Garcia, V. *et al.* Ferroelectric control of spin-polarization. *Science* **327,** 1106–1110 (2010).
22. Chen, C. T. *et al.* Experimental confirmation of the X-ray magnetic circular dichroism sum rules for iron and cobalt. *Phys. Rev. Lett.* **75,** 152–155 (1995).
23. Abrudan, R. *et al.* Structural and magnetic properties of epitaxial Fe/CoO bilayers on Ag(001). *Phys. Rev. B* **77,** 014411 (2008).
24. Noguès, J. *et al.* Exchange bias in nanostructures. *Phys. Rep.* **422,** 65–117 (2005).
25. Jullière, M. Tunneling between ferromagnetic films. *Phys. Lett. A* **54,** 225–226 (1975).
26. Bowen, M. *et al.* Nearly total spin-polarization in $La_{2/3}Sr_{1/3}MnO_3$ from tunneling experiments. *Appl. Phys. Lett.* **82,** 233–235 (2003).
27. Zhuravlev, M. Y., Sabirianov, R. F., Jaswal, S. S. & Tsymbal, E. Y. Giant electroresistance in ferroelectric tunnel junctions. *Phys. Rev. Lett.* **94,** 246802 (2005).
28. Kohlstedt, H., Pertsev, N. A., Rodriguez Contreras, J. & Waser, R. Theoretical current–voltage characteristics of ferroelectric tunnel junctions. *Phys. Rev. B* **72,** 125341 (2005).
29. Cao, D., Cai, M-Q., Hu, W. Y. & Xu, C-M. Magnetoelectric effect and critical thickness for ferroelectricity in Co/$BaTiO_3$/Co multiferroic tunnel junctions. *J. Appl. Phys.* **109,** 114107 (2011).
30. de Teresa, J. M. *et al.* Role of metal-oxide interface in determining the spin polarization of magnetic tunnel junctions. *Science* **286,** 507–509 (1999).
31. Valencia, S. *et al.* B. X-ray magnetic circular dichroism in reflection geometry: A tool for investigating surface magnetism in thin films. *J. Appl. Phys.* **104,** 023903 (2008).
32. Zhuravlev, M. Y., Vedyayev, A. V. & Tsymbal, E. Y. Interlayer exchange coupling across a ferroelectric barrier. *J. Phys.: Condens. Matter.* **22,** 352203 (2010).
33. Gonze, X. *et al.* A brief introduction to the ABINIT software package. *Z. Kristallogr.* **220,** 558–562 (2005).
34. Gonze, X. *et al.* ABINIT: First-principles approach of materials and nanosystem properties. *Comput. Phys. Commun.* **180,** 2582–2615 (2009).
35. Shao, Y. *et al.* Quantification of the Ti oxidation state in $BaTi_{1-x}Nb_xO_3$ compounds. *Ultramicroscopy* **110,** 1014–1019 (2010).
36. Garcia-Barriocanal, J. *et al.* Spin and orbital Ti magnetism at $LaMnO_3/SrTiO_3$ interfaces. *Nature Commun.* **1,** 82 (2010).
37. Fujii, T. *et al.* Large magnetic polarization of Ti^{4+} ions in $FeTiO_3$. *J. Magn. Magn. Mater.* **310,** e555–e557 (2006).
38. Brice-Profeta, S. *Etude de l'Ordre Chimique et Magnétique d'Oxydes Spinelles de Taille Nanométrique par Dichroïsme Magnétique Circulaire des Rayons X.* PhD thesis, Univ. Pierre et Marie Curie (2004).
39. Yu, P. *et al.* Interface ferromagnetism and orbital reconstruction in $BiFeO_3$–$La_{0.7}Sr_{0.3}MnO_3$ heterostructures. *Phys. Rev. Lett.* **105,** 027201 (2010).
40. Sefrioui, Z. *et al.* All-manganite tunnel junctions with interface-induced barrier magnetism. *Adv. Mater.* **22,** 5029–5034 (2010).
41. Jang, F. *et al.* Eight logic states of tunneling magnetoelectroresistance in multiferroic tunnel junctions. *J. Appl. Phys.* **102,** 044504 (2007).
42. Wang, J. & Li, Z. Y. Multiple switching of spin polarization injected into a semiconductor by a multiferroic tunneling junction. *J. Appl. Phys.* **104,** 033908 (2008).
43. Spaldin, N. A., Fiebig, M. & Mostovoy, M. The toroidal moment in condensed-matter physics and its relation to the magnetoelectric effect. *J. Phys.: Condens. Matter* **20,** 434203 (2008).
44. Oleinik, I. I., Tsymbal, E. Y. & Pettifor, D. G. Atomic and electronic structure of Co/$SrTiO_3$/Co magnetic tunnel junctions. *Phys. Rev. B.* **65,** 020401(R) (2001).
45. Bowen, M. *et al.* Absence of induced moment in magnetic tunnel junction barriers. *Phys. Rev. B* **73,** 012405 (2006).
46. Bouzehouane, K. *et al.* Nanolithography based on real-time electrically controlled indentation with an atomic force microscope for nanocontact elaboration. *Nano Lett.* **3,** 1599–1602 (2003).
47. Houzé, F., Meyer, R., Schneegans, O. & Boyer, L. Imaging the local electrical properties of metal surfaces by atomic force microscopy with conducting probes. *Appl. Phys. Lett.* **69,** 1975–1977 (1996).
48. Rodriguez, B. J., Callahan, C., Kalinin, S. V. & Proksch, R. Dual-frequency resonance-tracking atomic force microscopy. *Nanotechnology* **18,** 475504 (2007).
49. Grabis, J., Nefedov, A. & Zabel, H. Diffractometer for soft x-ray resonant magnetic scattering. *Rev. Sci. Instrum.* **74,** 4048–4051 (2003).

Acknowledgements

This study was partially supported by France-UK PHC Alliance program, the Triangle de la Physique contract 'OXISPINTRONICS', UK EPSRC EP/E026206/I, Region Île-de-France in the framework of C'Nano IdF, the European ESTEEM and the METSA networks and the European Research Council Advanced grant project 'FEMMES' (no. 267579). The ALICE diffractometer is funded through the BMBF Contract No. 05K10PC2. The research leading to these results has received funding from the European Community's Seventh Framework Programme (FP7/2007-2013) under grant agreement no. 226716. X.M. acknowledges support from a Herschel–Smith fellowship. We also thank N. Reyren, V. Cros and F. Petroff for discussions.

Author contributions

S.V., V.G., A.B. and M.B. designed the experiments. X.M., N.D.M., R.O.C., C.D., K.B. and S.F. were responsible for the preparation and characterization of the samples. A.C., V.G., K.B., A.B. and M.B. performed the magnetotransport measurements and data analysis. S.V., A.C., V.G., A.Gaupp, L.B., R.A. and F.R. performed the XRMS, XAS and XMCD measurements and treated and interpreted the data. A.C., V.G., K.B. and S.F. carried out the PFM characterization. L.B. and A.Gloter performed the STEM-HAADF studies, the EELS measurements and interpreted the data. L.B., A.Gloter and A.Z. carried out the first-principles calculations and interpreted the results. S.V. and M.B. wrote the manuscript. All authors contributed to the manuscript and the interpretation of the data.

Additional information

The authors declare no competing financial interests. Supplementary information accompanies this paper on www.nature.com/naturematerials. Reprints and permissions information is available online at http://www.nature.com/reprints. Correspondence and requests for materials should be addressed to M.B.

© 2011 Macmillan Publishers Limited. All rights reserved